Hierarchical structure of niobate nanosheets in aqueous solution

Daisuke Yamaguchi,[a]* Nobuyoshi Miyamoto,[a] Satoshi Koizumi,[a] Teruyuki Nakato[b] and Takeji Hashimoto[a]

[a]Advanced Science Research Center, Japan Atomic Energy Agency, Shirakata-Shirane 2-4, Tokai, Naka, Ibaraki 319-1195, Japan, and [b]Graduate School of Bio-Applications and Systems Engineering (BASE), Tokyo University of Agriculture and Technology, Japan. Correspondence e-mail: yamaguchi.daisuke@jaea.go.jp

The hierarchical structure of an aqueous dispersion of niobate nanosheets was explored by using a combined method of ultra-small-angle and small-angle scattering of neutrons and X-rays. The concentration of the sheets studied was in the range where the dispersion exhibits a liquid-crystal phase as evidenced by observation between crossed polarizers in a previous report. The scattering data covered a wide q scale of more than four orders of magnitude [$3 \times 10^{-4} \leq q \leq 10$ nm^{-1}, where $q = (4\pi/\lambda)\sin(\theta/2)$, λ and θ being the wavelength of the incident beam and the scattering angle, respectively], corresponding to the length scale $l = 2\pi/q$ from ~1 nm to ~20 µm. The scattering analyses provided information on the hierarchical structural elements including: (i) single nanosheets as a structure element (hierarchy I), (ii) parallel stacks of the sheets (hierarchy II), and (iii) spatial arrangements of the stacks (hierarchy III), in order of increasing length scale. Hierarchy II is closely related to the liquid-crystal nature of the dispersion in which the spacing and the persistence length, normal and parallel to the stack surface, respectively, were disclosed. Hierarchy III gives rise to the low-q upturn in the scattering profile, which may be characterized by mass-fractal-like power-law scattering behavior. This finding is a surprise from the viewpoint of the liquid-crystal nature of the dispersion, a possible model of which is proposed in the text.

1. Introduction

Crystals of the inorganic layered niobate $K_4Nb_6O_{17}$ have two remarkable properties. One is related to their photoelectrochemical and -physical functions. The semiconductive and photocatalytic nature inherent in the layered $K_4Nb_6O_{17}$ crystal has potential applications for electronic devices (Ogawa & Kuroda, 1995). The other property is related to the structure. The layered crystal is easily delaminated into unit layers and the exfoliated $[Nb_6O_{17}]^{4-}$ sheets (hereafter called 'nanosheets') have an outstanding structural feature (Miyamoto *et al.*, 2002; Miyamoto & Nakato, 2004). The $[Nb_6O_{17}]^{4-}$ nanosheet has a crystallographically determined constant thickness of 1.6 nm, while its lateral size ranges from submicrometres to several tens of micrometres, so that the aspect ratio, *i.e.*, the ratio of lateral size to thickness, is extremely large, ranging from 100 to tens of thousands (Miyamoto *et al.*, 2002). A huge aspect ratio like this has never been obtained for other kinds of inorganic nanosheets, such as those of clays (Pignon *et al.*, 1997). The huge nanosheets are ordered to form a liquid-crystalline phase, which is basically explained by Onsager's theory (Onsager, 1949), as evidenced by observation between crossed polarizers (Miyamoto & Nakato, 2004). However the detailed structure of the liquid crystal is not clarified yet. The high uniformity of the thickness of the nanosheets should also be stressed. The layered crystals are believed to be quantitatively delaminated into bilayers *via* cation exchange of interlayer K^+ ions for propyl-ammonium cations, which makes the thickness of the nanosheets monodisperse (Saupe *et al.*, 2000; Miyamoto *et al.*, 2002).

The objective of this study is to elucidate the self-assembled structure of the aqueous dispersion of the nanosheets in the liquid-crystal phase. Some basic parameters clarified in this study are summarized in Fig. 1. Part (a) illustrates the single nanosheet in the
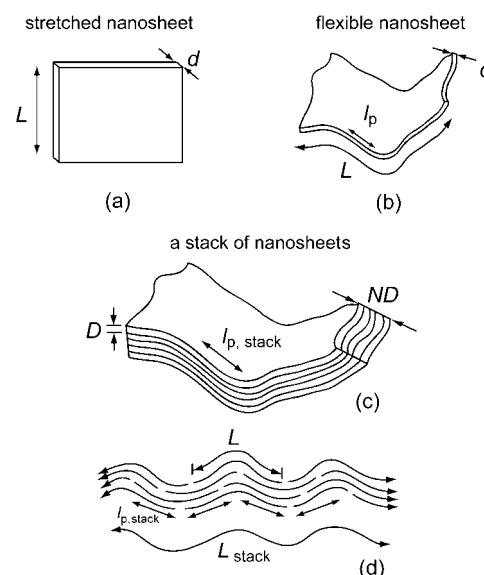
Figure 1
Summary of the basic parameters of the nanosheets. In part (b), L refers to the lateral contour length of the nanosheet.

stretched-out configuration which is characterized by lateral size (L) and thickness (d). The single nanosheet in water is flexible on a scale larger than the persistence length (l_p), whereas it is rigid and flat on a scale smaller than l_p as illustrated in part (b). In the lyotropic liquid-crystal phase, the sheets tend to stack parallel to each other with spacing D and stacking number N. The stacks will bend on a length scale larger than $l_{p,stack}$, the persistence length of the stack, as schematically shown in part (c). The sheets themselves will align parallel to one another along the lateral direction as well, as illustrated in part (d), so that the lateral contour length of the stacks, L_{stack}, could be much larger than L itself. $l_{p,stack}$ depends on ND and may be generally different from l_p. The stacks are considered to uniformly fill the space with some bending, splaying and twisting degrees of freedom.

The self-assembly of the sheets was explored in reciprocal space through a combination of ultra-small-angle neutron (USANS) and X-ray scattering (USAXS) and small-angle neutron (SANS) and X-ray scattering (SAXS) methods. The combined small-angle scattering (SAS) method, which utilizes all the scattering methods described above in 'concert', is anticipated to systematically unveil all the hierarchical structures of the given system, which is built up from the nanosheets having an extremely large aspect ratio over the length scale from ~1 nm to ~20 µm.

2. Experimental section

2.1. Specimen and scattering cells

The nanosheets employed in this study were exfoliated from a single crystal of $K_4Nb_6O_{17}$. For details of $K_4Nb_6O_{17}$ single-crystal formation and the subsequent exfoliation process see Miyamoto & Nakato (2004). The lateral dimension of the nanosheet evaluated by transmission electron microscopy was L (mean value) = 3.2 µm and σ/L (relative standard deviation) = 0.079. The definitions of L and σ are also given by Miyamoto & Nakato (2004). In the aqueous dispersion to be investigated in this work, the molar concentration of the nanosheets is 1.4×10^{-1} mol dm^{-3}, corresponding to 0.032 in volume fraction, provided the thickness of the nanosheet is 1.6 nm. Under observation by the naked eye or by optical microscopy, this specimen exhibits a uniform liquid-crystal phase without any phase separation.

The specimen was loaded into cells for the scattering measurements. The cell thickness was different depending on the type of irradiation: 1 mm for a neutron beam and 0.5 mm for an X-ray beam. The material of the cell was different as well: two plates of 1 mm thick quartz for a neutron beam and two sheets of 25 µm thick polyimide film (UPILEX, UBE Industries Ltd, Tokyo, Japan) for an X-ray beam. The cell was filled with the viscous aqueous dispersion of nanosheets by using a Pasteur pipette and then sealed with Teflon tape or Parafilm to avoid evaporation of water. Before the scattering measurement, the specimen was left for ~0.5 h after loading in the scattering cell to remove the effects of injection. In particular, USANS measurements were conducted as a function of time after the sample was injected into the scattering cell in order to check the time evolution of the structure. However, the scattering profile did not show any changes during the six months after preparation. In all the scattering experiments, the incident beam was parallel to the direction normal to the surface of scattering cell.

2.2. Scattering apparatus

The self-assembled structure of the aqueous dispersion of nanosheets was investigated by the combined SAS methods of USANS, USAXS, SANS and SAXS. Each scattering method was

assigned to cover a specific q range as will be indicated in Fig. 3 later. Here q is the magnitude of scattering vector defined by $q = (4\pi/\lambda)\sin(\theta/2)$, where λ and θ are the wavelength of the incident beam and the scattering angle, respectively.

USANS measurements were conducted using the S18 spectrometer at the Institute Laue–Langevin in Grenoble, France (Hainbuchner et al., 2000) and the PNO spectrometer at the research reactor JRR-3 at the Japan Atomic Energy Agency (JAEA) in Tokai, Japan (Aizawa & Tomimitsu, 1995), both of which are based on the Bonse–Hart-type double-crystal setup. S18 utilizes the 220 reflection of the Si monochromator crystal in order to select incident neutrons with $\lambda = 1.9$ Å, while PNO utilizes Si 111 and $\lambda = 2.0$ Å. All the scattering profiles were measured at ambient temperature and corrected for the background scattering and slit smearing (desmearing; Schmidt, 1965). The scattering profiles obtained with S18 and PNO were nearly identical, and therefore only the data from S18, which had a better signal-to-noise ratio, are presented here.

SANS measurements were conducted on the SANS-J-II spectrometer at JRR-3, JAEA (Koizumi et al., 2006). The sample-to-detector distances were set at 2 and 10 m, and the incident neutrons had $\lambda = 6.5$ Å and a wavelength dispersion ($\Delta\lambda/\lambda$) of 0.13. The data were corrected for background electric noise, background scattering from the empty cell and solvent (water), and nonuniformity of detector efficiency. After these corrections, the absolute scattering intensity was obtained by using a pre-calibrated secondary standard of irradiated aluminium (Schelten & Hendricks, 1975; Russell et al., 1988).

Both USAXS and SAXS experiments were carried out using the apparatuses at the Polymer Mechanics Laboratory, Department of Polymer Chemistry, Kyoto University, Kyoto, Japan. The incident X-rays had $\lambda = 1.54$ Å (Cu $K\alpha$ line). The details of the apparatuses have been described elsewhere [Koga et al. (1996) for USAXS and Fujimura et al. (1981), Hashimoto et al. (1981) and Suehiro et al. (1986) for SAXS]. The sample-to-detector distance was set at 330 mm for the SAXS measurements in this work. The data were corrected for air scattering, absorption, and slit-width and slit-height smearing for both USAXS and SAXS. Background scattering arising from thermal diffuse scattering (TDS) (Vonk, 1973) was subtracted from the SAXS data. The absolute intensities for SAXS and USAXS were obtained using the nickel-foil method (Hendricks, 1972).

2.3. A combined SAS profile on a common absolute scattering intensity scale

In order to construct a combined USANS, USAXS, SANS and SAXS profile on a common absolute intensity scale, e.g., on the intensity scale of neutron scattering, the absolute USAXS and SAXS scale must be further transformed to the absolute neutron scattering intensity scale. This transformation is considered to be straightforward, because the system comprises only two components (water and the nanosheets). In this case, SAXS and SANS have the same intensity distribution and only their absolute intensity levels are different. Thus we should be able to convert the SAXS profile into the SANS profile by a vertical shift of the SAXS profile on a logarithmic intensity scale to the SANS profile also on a logarithmic scale. In fact, we confirmed that the two profiles are superimposable with a significantly wide q range over which the two profiles are clearly overlapping, as will be shown in Fig. 3 later. Similarly, the absolute intensity of the USAXS profile was converted to that of the SANS profile with a significantly wide overlapping q range; the absolute intensity of the USANS profile was calibrated using the absolute intensity of the SANS profile with the aid of the significantly wide overlapping q range of the USAXS profile with the USANS profile
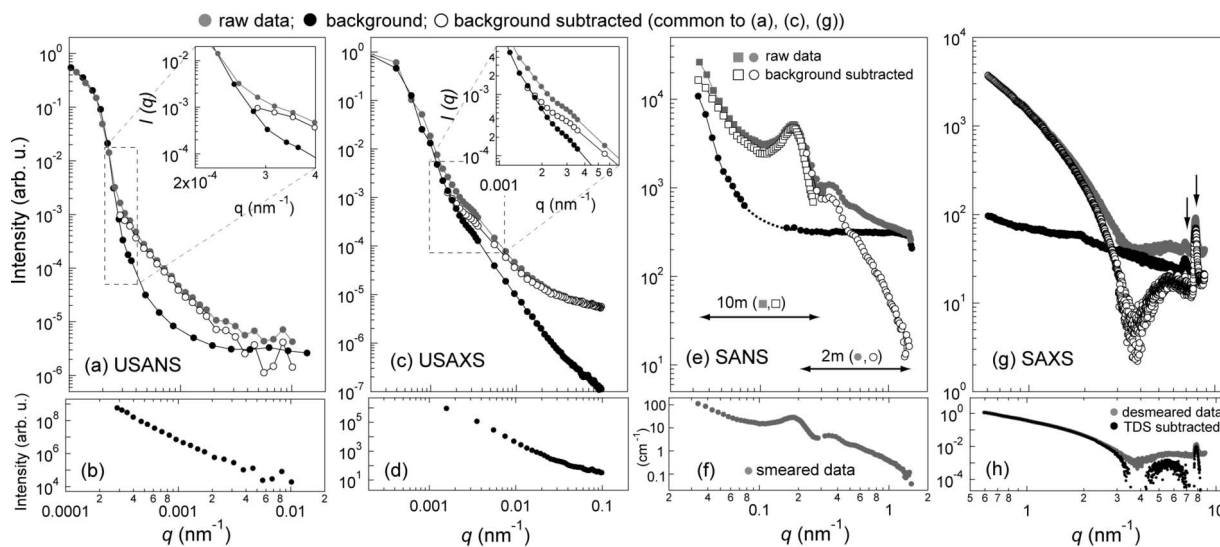
Figure 2
Scattering data: (a), (b) USANS; (c), (d) USAXS; (e), (f) SANS; and (g), (h) SAXS.

and the SANS profile on a logarithmic intensity scale, as will be also demonstrated later in Fig. 3.

The scattering in the q region of $3 \times 10^{-2} < q < 2$ nm^{-1} was measured with the SANS apparatus, although most of this q range is also accessed by SAXS. The main reason for the choice of the SANS apparatus for this q range is that the neutron beam has a higher transmittance for the nanosheets compared to the X-ray beam. However, for q larger than 2 nm^{-1}, the X-ray beam is superior to the neutron beam because of the high incoherent scattering from water for neutrons in this q range. Turning our attention to the ultra-small-angle region, neutrons have an absolute advantage for the q range smaller than ~1 $\times$ 10^{-3} nm^{-1}, which is inaccessible to USAXS apparatus. On the other hand, for the q range from 1 $\times$ 10^{-2} to 1 $\times$ 10^{-1} nm^{-1}, USAXS is superior to USANS because of the higher luminosity and thereby better signal-to-noise ratio of USAXS compared to USANS. Thus, the complementary use of neutrons and X-rays as well as that of ultra-small-angle scattering (USAS) and SAS are quite indispensable in this study.

3. Results

3.1. USANS data treatment

Fig. 2(a) shows the background profile (dark circles) together with the USANS scattering profiles of the specimen before (gray circles) and after the background subtraction (unfilled circles). Note hereafter that all of the scattering profiles from specimen are corrected for transmission, and therefore they are directly compared with background scattering. Over the q range from 3 $\times$ 10^{-4} to 3 $\times$ 10^{-3} nm^{-1}, the raw scattering data from the specimen have high enough intensity compared with the background as evidenced by the fact that the data before and after the background subtraction are almost identical, and therefore the data in this region seem very reliable. Fig. 2(b) shows the desmeared scattering profile obtained by desmearing the background-subtracted scattering profile.

3.2. USAXS data treatment

The data-treatment process for the USAXS measurements is essentially identical to that of USANS. Fig. 2(c) shows the background profile together with the USAXS scattering profiles of the

specimen before and after background subtraction. The scattering data at $q \geq 1.5 \times 10^{-3}$ nm^{-1} were sufficiently greater than those of the background scattering and are therefore considered to be reliable. Fig. 2(d) shows the desmeared scattering profile.

3.3. SANS data treatment

Although the individual nanosheets themselves are highly anisotropic in shape, the SANS scattering pattern taken with the incident neutron beam normal to the cell surface was circularly symmetric with respect to the incident beam. Therefore the two-dimensional scattering pattern of the specimen was circularly averaged and transformed into the one-dimensional scattering intensity profile $I(q)$ as shown in Fig. 2(e). In Fig. 2(e) two data sets are plotted together; one is measured at the sample-to-detector distance of 10 m and the other is measured at 2 m. These two data sets overlap each other in the q range from 0.2 to 0.3 nm^{-1}. Below 0.03 nm^{-1} the instrumental resolution is poor and above 1 nm^{-1} the signal-to-noise ratio was low. Therefore the SANS q range was limited to 0.03–1 nm^{-1}. The data
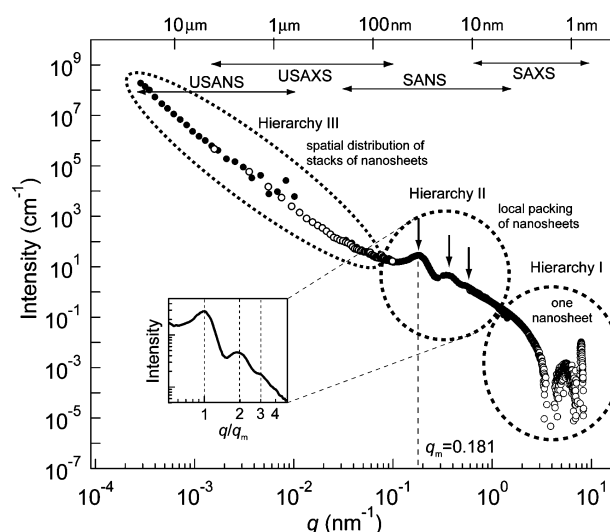
Figure 3
Combined scattering profile of an aqueous dispersion of niobate nanosheets.

corrected for the background scattering are plotted in Fig. 2(f). Since the scattering was obtained by using an incident beam with a circularly symmetric intensity distribution around the beam axis, the SANS profile was not desmeared. The desmeared SAXS profile showed that the q values at the SAXS scattering maxima were identical to those of the SANS profile (although the corresponding data are not shown here). This indicates that the smearing effect on the SANS is so small that the peak positions are not affected, although the peak breadths may be affected.

3.4. SAXS data treatment

The SAXS profile is plotted together with the background (*i.e.*, air scattering) in Fig. 2(g). In this q range the scattering from the specimen is characterized by the intensity minimum around $q \simeq 3.7$ nm^{-1}, which became fairly pronounced after the background-scattering subtraction. Note that there also exist two peaks at high q on both the scattering profiles from the specimen and the background (as marked by arrows at $q = 6.9$ and 7.9 nm^{-1}). The peak located at $q = 6.9$ nm^{-1} was cancelled out by the background subtraction, and thereby attributed to the background. On the other hand, the other peak located at $q = 7.9$ nm^{-1} was left even after the background subtraction. The spacing estimated from the peak at $q = 7.9$ nm^{-1} was 0.79 nm. This value is close to 0.76 nm, which corresponds to one of the lattice spacings of the two-dimensional structure of the nanosheet. Thus, we assigned the peak at $q = 7.9$ nm^{-1} to this lattice spacing. The SAXS data obtained after the background-scattering subtraction were corrected for the slit geometry. The desmeared scattering profile is presented in Fig. 2(h). The desmeared profile was further corrected for the background scattering arising from TDS (Vonk, 1973). After the correction for TDS, a broad maximum located in the q range 4–8 nm^{-1} becomes much more conspicuous.

3.5. A combined scattering profile

All the scattering profiles shown in Fig. 2(b), (d), (f) and (h) are now combined together by using the method described in §2.3. The combined scattering profile presented in Fig. 3 has the absolute intensity for the neutron scattering as detailed in §2.3. The combined profile is divided into the following three parts which represent different 'hierarchical' structural levels in order of increasing length scale: (i) the first hierarchy represents the single nanosheets, speci-

fically a broad maximum located in the q range 4–8 nm^{-1} representing the sheet thickness d; (ii) the second hierarchy represents the local packing of the sheets with the spacing D and the later extensions $l_{p,stack}$, as shown in Fig. 1(c) and (d); and (iii) the third hierarchy represents a spatial organization of the stacks of sheets over the length scale 0.1–10 μm, where the scattering exhibits power-law behavior. Details of these three hierarchies will be discussed below.

4. Analysis and discussion

4.1. Hierarchy I

In Fig. 4, the combined scattering profile is compared with the calculated scattering function of the particle form factor $P(q)$ for randomly oriented thin discs of thickness d and radius R satisfying the criterion $d \ll R$ (Guinier & Fournet, 1955),

$$P(q) = 4V^2\rho_0^2\left(\frac{2}{q^2R^2}\right)\left[1 - \frac{J_1(2qR)}{qR}\right]\frac{\sin^2(qd/2)}{(qd/2)^2}, \quad (1)$$

where V is the volume of the particle, ρ_0 is the scattering contrast between the particle and the surrounding medium and J_1 is the first-order Bessel function. In the model the nanosheet is approximated as a thin circular disc, based on the principle that at large q the scattering would arise from single nanosheets in the stacks of the sheets with lateral dimension of $l_{p,stack}$ defined in Fig. 1(c) or (d). In this case $2R$ approximately corresponds to $l_{p,stack}$.

The best fit of $P(q)$ (shown by the solid line) with the measured profile was obtained for the high-q range of $q \geq 1$ nm^{-1}, from which the thickness of the individual sheet d was estimated to be 1.6 nm. At $q < 1$ nm^{-1} $P(q)$ deviates from the measured profile, which is primarily due to intersheet interference effects. $P(q)$ shows a power-law behavior with exponent 2 over a wide q range of $3 \times 10^{-2} < q < 1$ nm^{-1}, indicative of thin discs.

4.2. Hierarchy II

In the q range 0.1–1 nm^{-1} characterizing hierarchy II, there are at least three scattering peaks which are found at integer multiples of the first-order peak position q_m, suggesting that the nanosheets are regularly stacked parallel to one another and thereby into a lamellar phase. This locally parallel packing of the nanosheets is the origin of the liquid-crystalline texture for the aqueous dispersion of the sheets. The parallel packing in turn should be primarily attributed to the excluded volume effect of the sheets with a very large aspect ratio l_p/d in Fig. 1(b) (Onsager, 1949).

We can analyze the uniformity of the spacing D on the basis of paracrystal analysis (Hosemann & Bagchi, 1962; Hashimoto *et al.*, 1985). For the lamellar phase one can discern the nth order diffraction if $gn \leq 0.35$ where g is the paracrystal distortion parameter defined by $g = \Delta D/\overline{D}$, where ΔD is the standard deviation of D from
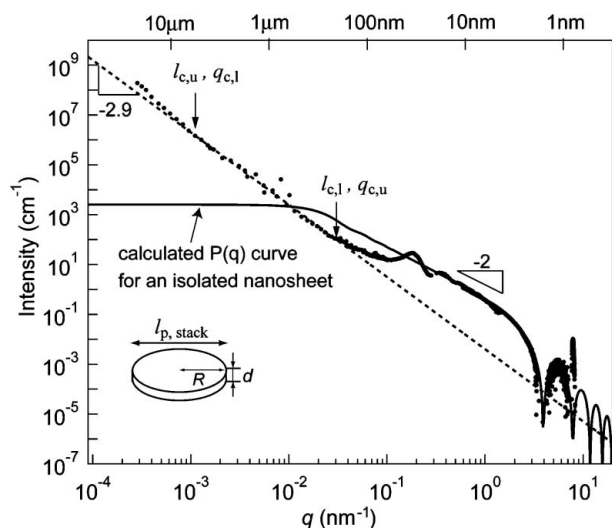
Figure 4
Analysis of the scattering profile of an aqueous dispersion of niobate nanosheets.
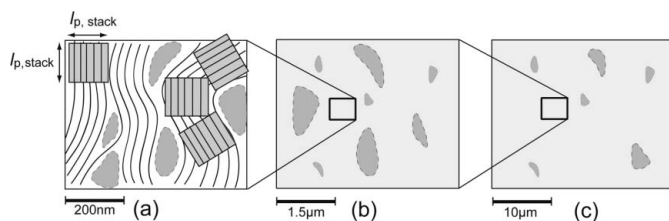
Figure 5
Schematic illustration of nanosheet stacks coexisting with water regions (regions enclosed by broken lines).

the average value $\overline{D}$. Since up to third-order peaks are discerned we can conclude that $0.088 < g < 0.12$, a quite uniform spacing.

The average spacing $\overline{D}$ is determined to be 34.6 nm from the position of the interference peak ($q_m = 0.181$) by using the relation

$$\overline{D} = 2\pi/q_m. \tag{2}$$

Then, from the ratio of d (= 1.6 nm, as obtained in §4.1) to $\overline{D}$, the local volume fraction of the nanosheets within the stacks, ϕ_l, is evaluated as 0.046. Here an important question comes up; the local concentration of the nanosheets ($\phi_l = 0.046$) is considerably larger than the volume expected from the stoichiometry of the sample preparation ($\phi = 0.032$, cf. §2.1). This implies that only ca 70% of the water was used for swelling the distance of the nanosheets, while the residual ca 30% of water should be somewhere else, but within the system. Nevertheless, the aqueous solution observed by polarized optical microscopy shows a liquid-crystalline phase uniformly extended everywhere in the sample space: there are no possibilities of a biphase coexistence where the anisotropic phase coexists with isotropic phase. Under this situation, the following simple idea may occur. The residual water splits into regions composed only of water (water regions) inside the liquid-crystalline phase, due to the undulation of the stacks of the sheets as depicted schematically in Fig. 5(a). The spatial arrangements of the water regions may be fractal-like and thereby contribute to the power-law scattering in hierarchy III.

4.3. Hierarchy III

Over the q range from 1×10^{-3} to 3×10^{-2} nm^{-1}, the specimen exhibits a power-law scattering behavior with a power-law exponent close to -2.9. The power-law scattering behavior has been often related to two kinds of fractal dimensions; one is the mass fractal dimension d_f and the other is the surface fractal dimension d_s (Freltoft et al., 1986). Each fractal dimension is related to the scattering power-law behavior, $I(q) \propto q^{-\alpha}$, by

$$\alpha = d_f \quad (1 \leq d_f \leq 3) \tag{3}$$

and

$$\alpha = 6 - d_s \quad (2 \leq d_s \leq 3). \tag{4}$$

The exponent of $\alpha = 2.9$ is attained only by equation (3). Therefore we attempt to interpret this power-law scattering by the concept of a mass fractal distribution of the water regions with a lower cut-off q value, $q_{c,l}$, of $\sim 1 \times 10^{-3}$ nm^{-1} and an upper cut-off q value, $q_{c,u}$, of $\sim 3 \times 10^{-2}$ nm^{-1}. The corresponding upper cut-off length $l_{c,u} = 2\pi/q_{c,l}$ and the lower cut-off length $l_{c,l} = 2\pi/q_{c,u}$ are ~ 6.3 µm and ~ 200 nm, respectively.

Fig. 5 schematically illustrates a mass fractal model. On the length scale where the local stacks of the nanosheets are visible as shown in part (a), a spatial arrangement of the water regions may be discernible as a consequence of undulation of the stacks of the sheets with persistence length $l_{p,stack}$. If we lower the magnification or look at the texture on a much larger scale, as schematically shown in part (b), the area shown in part (a) may appear homogeneous, but we may still find water regions having a larger size than in part (a) but distributed similarly to the water regions shown in part (a). If we further lower the magnification as schematically shown in part (c), the area shown in part (b) may appear homogeneous, but we may still find water regions having a larger size than in part (b) but distributed similarly to the water regions shown in part (b). In a transmission polarized optical microscopy image, the water regions and the liquid-crystalline regions may be overlapped along the incident beam path due to the

large sample thickness (~0.2 mm), so that the image may show a uniform liquid-crystal phase.

5. Conclusion

The structure of an aqueous dispersion of $[Nb_6O_{17}]^{4-}$ nanosheets having a particular stretched-out lateral size (3.2 µm) and volume fraction (0.032) was explored by using ultra-small-angle and small-angle scattering methods using both neutron and X-ray beams. Although this specimen was previously considered to be a uniform liquid-crystalline phase, the scattering studies revealed that there exist some concentration fluctuations of the nanosheets, giving rise to water-rich regions, which originate from undulation of stacks of the nanosheets. The spatial arrangement of the water regions in the liquid-crystalline phase may be characterized by a mass fractal. The thickness of individual nanosheets as well as the spacing between the nanosheets and its uniformity were also elucidated by the combined SAS method proposed in this study.

The authors are indebted to Dr Kenji Saijo for providing access to the USAXS and SAXS apparatus at the Polymer Mechanics Laboratory at Kyoto University and for his great help during the experiments. We gratefully acknowledge Professor H. Rauch for providing access to the USANS instrument at the S18 beamline at ILL, Grenoble, France, and Dr R. Loidl for his help during the USANS experiments. We thank Professor T. Kawakatsu for a useful discussion concerning the fractal structure.

References

Aizawa, K. & Tomimitsu, H. (1995). *Physica B*, **213–214**, 884–886.
Freltoft, T., Kjems, J. K. & Sinha, S. K. (1986). *Phys. Rev. B*, **33**, 269–275.
Fujimura, M., Hashimoto, T. & Kawai, H. (1981). *Mem. Fac. Eng. Kyoto Univ.* **43**, 224–239.
Guinier, A. & Fournet, G. (1955). *Small Angle Scattering of X-rays*. New York: Wiley.
Hainbuchner, M., Villa, M., Kroupa, G., Bruckner, G., Baron, M., Amenitsch, H., Seidl, E. & Rauch, H. (2000). *J. Appl. Cryst.* **33**, 851–854.
Hashimoto, T., Suehiro, S., Shibayama, M., Saijo, K. & Kawai, H. (1981). *Polym. J.* **13**, 501–506.
Hashimoto, T., Tanaka, H. & Hasegawa, H. (1985). *Macromolecules*, **18**, 1864–1868.
Hendricks, R. W. (1972). *J. Appl. Cryst.* **5**, 315–324.
Hosemann, R. & Bagchi, S. N. (1962). *Direct Analysis of Diffraction by Matter*. Amsterdam: North-Holland.
Koga, T., Hart, M. & Hashimoto, T. (1996). *J. Appl. Cryst.* **29**, 318–324.
Koizumi, S., Iwase, H., Suzuki, J., Oku, T., Motokawa, R., Sasao, H., Tanaka, H., Yamaguchi, D., Shimizu, H. M. & Hashimoto, T. (2006). *Physica B*, **385–386**, 1000–1006.
Miyamoto, N. & Nakato, T. (2004). *J. Phys. Chem. B*, **108**, 6152–6159.
Miyamoto, N., Yamamoto, H., Kaito, R. & Kuroda, K. (2002). *Chem. Commun.* pp. 2378–2379.
Ogawa, M. & Kuroda, K. (1995). *Chem. Rev.* **95**, 399–438.
Onsager, L. (1949). *Ann. NY Acad. Sci.* **51**, 627–659.
Pignon, F., Magnin, A., Piau, J.-M., Cabane, B., Lindner, P. & Diat, O. (1997). *Phys. Rev. E*, **56**, 3281–3289.
Russell, T. P., Lin, J. S., Spooner, S. & Wignall, G. D. (1988). *J. Appl. Cryst.* **21**, 629–638.
Saupe, G. B., Waraksa, C. C., Kim, H.-N., Han, Y. J., Kaschak, D. M., Skinner, D. M. & Mallouk, T. E. (2000). *Chem. Mater.* **12**, 1556–1562.
Schelten, J. & Hendricks, R. W. (1975). *J. Appl. Cryst.* **8**, 421–429.
Schmidt, P. W. (1965). *Acta Cryst.* **19**, 938–942.
Suehiro, S., Saijo, K., Ohta, Y., Hashimoto, T. & Kawai, H. (1986). *Anal. Chim. Acta*, **189**, 41–56.
Vonk, C. G. (1973). *J. Appl. Cryst.* **6**, 81–86.